SEDIMENTOLOGY the journal of the International Association of Sedimentologists

Sedimentology (2022) **69**, 2348–2366 doi: 10.1111/sed.12995

Middle to late Holocene sedimentary filling history of the Sebkha el Melah in south-eastern Tunisia

MARIEM BEN AMEUR*,† , SAMEH MASMOUDI‡, HAMDI OMAR*,§, IMEN OUAMENI¶, MOUNIR MEDHIOUB‡ and CHOKRI YAICH*,†
**Engineering School of Sfax, Road of Sokra km 4, Sfax, 3038, Tunisia (E-mail: mariembenameur325@gmail.com)*
†GEOGLOB Laboratory, FSS (LR13ES23), University of Sfax, Road of Sokra, Sfax, 3028, Tunisia
‡Laboratoire de Spectroscopie et Caractérisation Optique des Matériaux La.S.C.O.M (LR17 ES 09), FSS, University of Sfax, Route de Soukra, BP 802, Sfax, 3028, Tunisia
§Sedimentary Petrology Laboratory, Liège University, Allée du Six Août, 12, Liège, 4000, Belgium
¶Faculty of Sciences of Sfax, University of Sfax, Road of Sokra, Sfax, 3028, Tunisia

Associate Editor – Nathan Sheldon

ABSTRACT

The sedimentological and geochemical properties of a 146 cm long sediment core collected from Sebkha el Melah (Ml core) in south-eastern Tunisia have been used to infer the genesis and evolution of the Sebkha el Melah over the last 5000 years. Two main sedimentary units have been defined: a huntite [$Mg_3Ca(CO_3)_4$] unit at the bottom of core Ml is covered by a second unit made up of siliciclastic and evaporitic materials. The huntite level is synchronous with Holocene marine transgression, which was followed by a regression of about 5300 years BP. Geochemical data (major and trace element), magnetic analyses, grain-size distribution and microtexture of quartz grains were performed to assess the sediment provenance. The upper unit of Ml core is characterized by alternations between fluvial, aeolian and evaporite deposits. Redox proxies displaying marked Fe/Ca and Rb/S peaks, in addition to high magnetic susceptibility (MS) values, polymodal grain-size frequency curves, as well as sub-angular grains with V-shaped percussion cracks, are suggestive of palaeohydrological events. In contrast, a decreasing trend in the low MS values, bi-modal grain-size frequency curves as well as well-rounded quartz grains with crescent percussion marks would indicate enhanced aeolian sand input in the sebkah el Melah sequence. Moreover, geochemical proxies suggest formation of evaporite facies under a strongly warm climate contemporary with marine intrusion.

Keywords Climate change, facies alternation, Holocene, sebkha, south-east Tunisia.

INTRODUCTION

Dryland lakes can capture sensitive changes in precipitation/evaporation balance by adjustments in water level and salinity. The south-east of Tunisia teems with sebkhas. Most of them are filled with sediments and are basically dry at the present time. Owing to their special geographical position (in desert margins), these sebkhas exhibit the interactions between the aeolian processes of the arid part and fluvial processes of the semi-arid part. These closed basins provide a very good record of palaeohydrological and palaeoclimatic proxy data (Tyler *et al.*, 2006).

The largest sebkha in south-eastern Tunisia, called el Melah (Fig. 1), has already been the central focus of multiple studies. From this

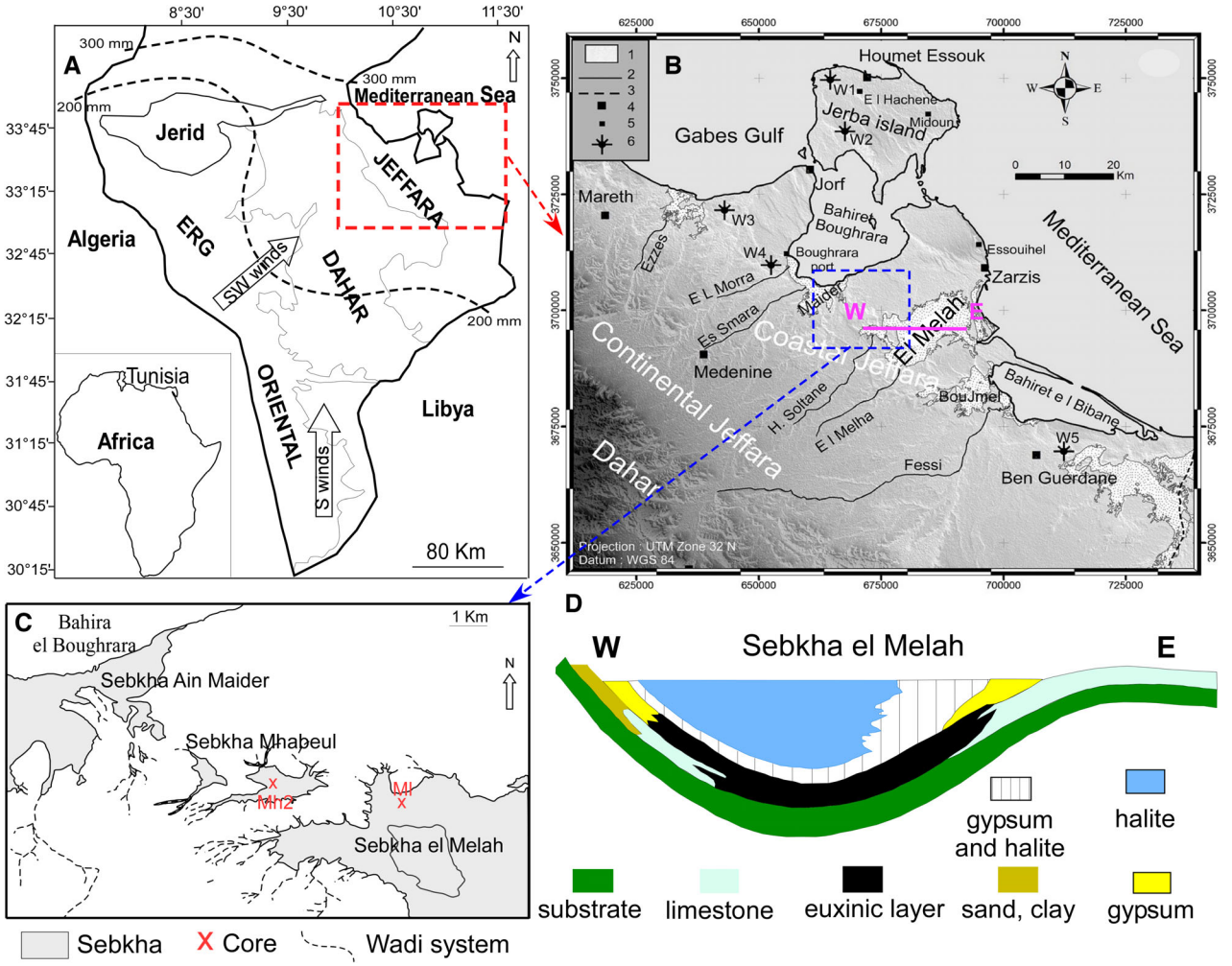

Fig. 1. Geographical settings. (A) Map of Southern Tunisia; the red square denotes the location of the study area – outlined in red on the map (B) and shown in detail in (C) – and iso-precipitation lines mark the annual rainfall. (B) From Ghedhoui *et al.* (2016): Geography of the studied area (N315°E SRTM DEM hill-shading base map) (1. Sebkhas; 2. Oued/Talweg; 3. Tunisian–Libyan border; 4. City; 5. Village; 6. Petroleum Well). (C) Displays the position of the Ml and Mh2 (Ben ameur *et al.*, 2021) cores. (D) Schematical transect through Sabkha el Melah sedimentary fillings.

perspective, earlier works tackled a variety of its aspects, such as the depositional environment evolution in relation to sea-level fluctuations, the interpretation of fossil evaporites, evaporite mineralogy, geology and geochemistry, sedimentology, carbonate biodiagenesis, radiocarbon dating and huntite formation (Florida, 1971; Fontes & Perthuisot, 1971, 1973; Perthuisot, 1971, 1974, 1975; Perthuisot *et al.*, 1972, 1990; Busson & Perthuisot, 1977; Abichou, 2002; Lakhdar *et al.*, 2006). These studies provided a certain understanding of the el Melah basin evolution from opened lagoon during the Flandrian Transgression (6000 to 4000 years BP) into sebkha–lagoon system during the Flandrian Regression (4000 to 3500 years BP), and a closer investigation of geochemical characteristics of the evaporite minerals of the near-surface sediments.

The scarcity of studies on palaeoclimate reconstitutions from such environments, which are the best record of the sedimentary filling history, was the basic catalyst and motivation for the present study. This paper also aims to explore sebkha basin sediments as sites for a deeper and thorough understanding of the complexity of the environmental drivers that lead to changes in these saline systems, as well as long-term sedimentological variations in response to climate variability.

STUDY AREA

The Sebkha el Melah, a large depression located at the northern edge of the 'Jeffara coastal plain', is roughly oriented north-east/south-west with 150 km^2 in surficial extension. It is 30 km long and 10 km wide, and lies between 1 m and 3 m above sea level (Fig. 1). Its surface is flat and mostly dry. The Jeffara extends over all of the coastal plain from Gabes (south-eastern Tunisia) to the Libyan border. It is limited to the west by the Matmata and Dahar Mountains and to the east by the Mediterranean Sea. The geodynamic structure of the coastal Jeffara reveals 'relay zones' of a major north-west/south-east right-lateral strike–slip transtensive fault that affected the Holocene and Villafrachian deposits (Ghedhoui *et al.*, 2016).

The coastal Jeffara is characterized by a pre-Saharan arid to a semi-arid climate. The average annual temperature is 20°C, with a maximum of 40°C during August. Annual precipitation amounts to less than 200 mm. The Saharan wind called sirocco (locally known as chehili or ghibli), is most frequent in spring and summer (Bousnina, 1990). It blows from the south and south-west or deviates to the south-east. Its turbulent movement is frequently responsible for suspending fine sand in the atmosphere (Fig. 1A).

The Sebkha el Melah is fed in the western part by two major Wadis, namely Hassi Soltane and el Melah (Fig. 1B), which originate from the mountainous chain of Matmata (Dahar; Abichou, 2002). There are numerous other local rivulets (or small local wadis) feeding Sebkha el Melah (Fig. 1B). In recent times, these dryland surfaces have been extensively investigated as salt pans for commercial salt production.

The previous sedimentological and geochemical studies of the Sebkha el Melah (Perthuisot, 1971, 1975; Perthuisot *et al.*, 1990) allowed recognition of the facies distribution during the Würm–Holocene (Fig. 1D). Thereby, the Sebkha el Melah sequence is composed by: (i) a biodetrital carbonate layer; (ii) a gypsum layer, which disappears in the deepest parts of the basin; (iii) a halite layer which reaches 27 m thickness. One of the most striking features of this series is the presence of a huntite horizon, which lies just underneath the gypsum bed; this level is located in the peripheral parts of the saline basin (mostly eastern and western parts). The huntite horizon laterally passes to magnesite-bearing euxinic deposits in the deepest parts of the basin (Perthuisot *et al.*, 1990). According to Fontes & Perthuisot (1971, 1973), a sample of huntite deposit collected from the eastern part of the saline basin (where the Ml core was collected) yielded a ^{14}C age of 5330 ± 170 years BP. Resting on the huntite level datation, the Sebkha el Melah core covers the last 5300 years.

SAMPLING AND ANALYTICAL METHODS

A 146 cm long core (Ml: 33°23′37.68″N; 10°55′37.80″E) was collected from the outlying parts of the Sebkha el Melah (Fig. 1C). The core was sampled at 0.5 cm intervals for magnetic susceptibility (MS), geochemical and sedimentological analysis. Samples were packed into 10 cm^3 cylindrical Perspex® pots for MS analysis. This parameter is expressed in SI (International System of Units) and is provided with an accuracy of 95% at the confidence level. Magnetic susceptibility analysis was carried out by the Bartington MS2B probe (Bartington Instruments Limited, Witney, UK) in the laboratory of Geoglob, National Engineering School of Sfax. Geochemical composition was determined separately for bulk samples and water soluble fraction through various analytical techniques. Concentrations of Na and K in leachate were measured by flame photometer for 292 samples. Major element (Si, Al, Ti, Ca, Mg and S) and trace element (Rb and Zr) proportions of 17 sampled levels were specified using X-ray fluorescence (XRF). The $CaCO_3$ content of sediment samples was determined by the Bernard calcimeter method.

The heavy minerals were separated by decantation under gravity with bromoform (2.89 g cm^{-3}) and analyses were performed on the >50 μm fraction of each sample. The separated heavy minerals were identified using a binocular microscope.

Grain-size analysis was conducted using a 'Fritsch Analysette MicroTech Plus' laser granulometer (Fritsch International, Idar-Oberstein, Germany) which has a measurement range of 0.01 to 2000 μm. Statistical parameters of mean, standard deviation, skewness and mode were estimated using the graphic expressions of Folk & Ward (1957) once the percentiles are converted to phi units. The lognormal distribution on the cumulative probability coordinate was used to separate the multimode from the grain-

size distribution, according to the method described by Qin *et al.* (2005).

Quartz grains (from 12 sediment samples at different depths in the core) of the sand fraction (2 to 3 φ as well as the 3 to 4 φ) were examined for quartz morphology and microtexture analyses. Sand grains were washed in cold 10% HCl to clean them from carbonate-clayey and ferruginous contamination, then washed with distilled water and finally dried at room temperature. Morphoscopic groups were explored following the method of Cailleux (1942). Grains were divided into angular, blunt-shining AL/EL ('anguleux et emoussées-luisants', usually associated with transport in water), and moderately rounded and round-matt grains 'EM/RM' ('ronds-mats' associated with aeolian transport). Scanning electron microscopy imaging was conducted using a JEOL-JSM-5400 LV apparatus (JEOL Limited, Tokyo, Japan) at the «Entreprise Tunisienne d'Activité Pétrolière». The quartz grains chosen for examination had a diameter between 50 µm and 315 µm. The surface feature recognition and interpretation were performed in accordance with the concepts of Krinsley & Doornkamp (1973), Le Ribault (1977), Mahaney (2002), Kenig (2006) and Vos *et al.* (2014).

RESULTS

Sediment properties

Sediment texture and grain-size distribution records

The sediment profile of Ml core was divided into two different lithological units (Fig. 2). The lower unit I (146 to 120 cm) is a white mud

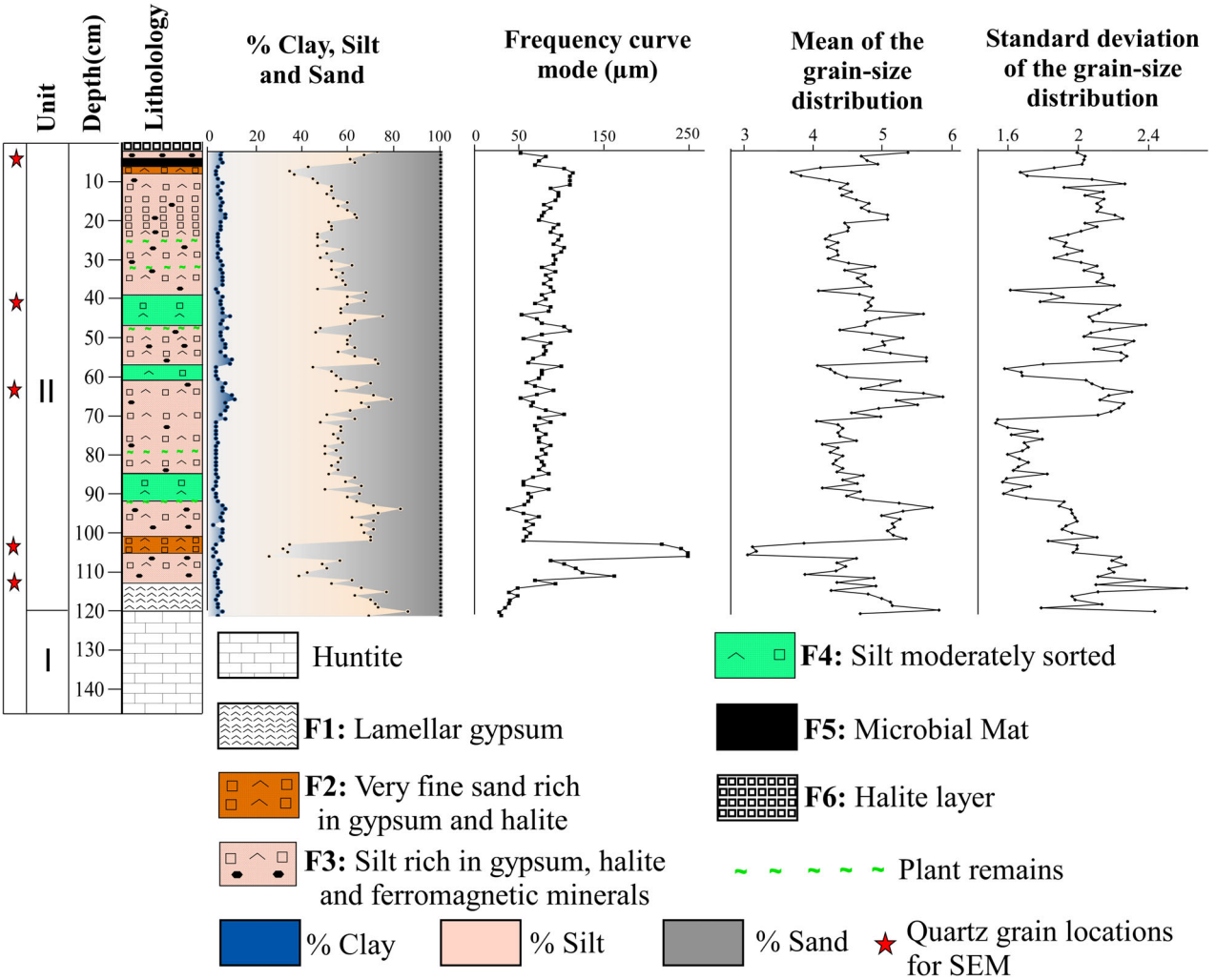

Fig. 2. Lithology and granulometry parameters of the Ml core.

consisting of a very pure huntite [$Mg_3Ca(CO_3)_4$]. Sediment at 0 to 120 cm of depth consists of alternating laminae of grey and dark grey silt (Unit II).

Sediments from Sebkha el Melah contain 14 to 74% sand, 32 to 80% silt and 2 to 11% clay (Fig. 2). The silt–sand-boundary-curve shape is consistent with the curves of standard deviation of the grain-size distribution. Basically, when the silt proportion is more important, sediment is poorly sorted, but better sorted with the increasing sand content.

The modal grain-size exhibits less variability from the surface up to 101 cm deep where the values vary between 37 μm and 114 μm, with an average grain diameter (Mz) mostly ranging from 4 to 5 φ, indicating very coarse silts. However, from 102 to 105 cm deep, modal grain-size sharply increases reaching a maximum of 248 μm, as depicted in Mz values reaching 3 to 3.8 φ fine sands. From 113 cm depth, the modal grain size tends to the lowest recorded values (28 to 49 μm) coinciding with Mz values between 4.6 φ and 5.8 φ, which indicates coarse and very coarse silts, respectively.

Sediment partitioning based on grain-size distributions

Grain-size distributions from Sebkha el Melah sediments consist of strongly polymodal mixtures and sometimes bimodal distributions. Indeed, very poorly sorted sediments always present polymodal grain-size frequency distribution curves, whereas moderately sorted sediments exhibit bimodal and trimodal grain-size frequency curves (Fig. 3).

The partitioning of the frequency curves of samples from 109 to 114 cm, 62 to 69 cm, 46 to 52 cm, 30 to 36 cm, 22 to 27 cm, 12 to 17 cm and 3 to 5 cm deep, is characterized by high sorting values (>2) and relatively high MS. All frequency distribution curves display four modal patterns (modes), including particle sizes ranging between 0.07 μm and 500 μm. Thereby, the four components (four modal peak) C1, C2, C3 and C4 vary within ranges of 0.07 to 0.7 μm, 0.54 to 8 μm, 6.2 to 44 μm and 74 to 500 μm, respectively. The relative percentages of C1, C2 and C3 vary between 2 to 4%, 3 to 27% and 22 to 36%, respectively. The highest modal peak C4 (primary modal peak) displays the dominant 53 to 64%.

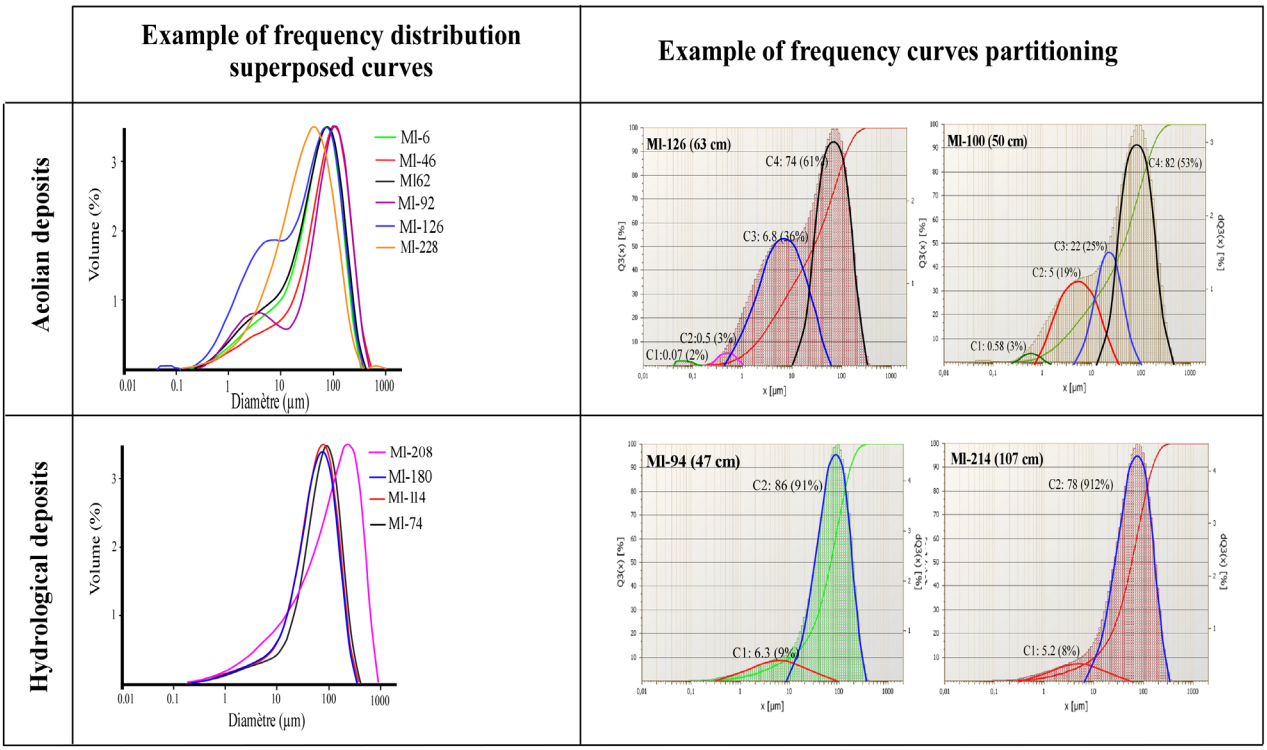

Fig. 3. Recognition of hydrological and aeolian deposits from frequency distribution superposed and partitioning curves during the last five millennia.

Several grain-size frequency curves of certain known sediments were selected (Fig. 3) in order to interpret the bimodal and trimodal pattern of Ml core samples. These samples, 102 to 105 cm, 86 to 91 cm, 56 to 59 cm and 37 to 40 cm deep, are moderately sorted and characterized by low MS. All samples contain two major grain-size components C1 and C2 with dominant modal sizes of 0.57 to 6.3 μm and 60 to 220 μm, respectively. The relative percentages of C1 and C2 vary within ranges of 3 to 10% and 67 to 91%, respectively. Indeed, intermediate components appear in some samples displaying a modal size of less than 25 μm (for example, Ml-208 sample, Fig. 3).

Morphoscopic and microtexture analyses of quartz grains

Morphoscopy and microtexture analyses of quartz grains are extremely useful in terms of determining sediment provenance from each depositional environment. Samples from the Ml core at different depths show both aeolian and fluvial origins.

Quartz grains were selected from levels where the MS values are relatively high (samples from 4 cm, 32 cm, 62.5 cm and 112 cm depths). The deposits include mainly AL/EL grains (Fig. 4A), but are accompanied with a lower proportion of moderately rounded grains (EM). Figure 4B to D reveal the scanning electron micrographs of the quartz grains from 4 cm (Ml 8), 62.5 cm (Ml 125) and 112 cm (Ml 224) depth exhibiting angular and sub-angular grains. V-shaped percussion cracks and conchoidal fractures forming arcuate and straight steps (grooves) are the most commonly observed features. They are produced by a powerful impact or pressure on the grain surface. These microtextures could have been formed during transport by fluvial streams (Fig. 4).

Samples from 40 cm, 78 cm and 103 cm depths, where MS values are very weak, unveil a distinct change in quartz grain morphoscopy (Fig. 5). Nearly the entire deposit is formed of matt and mostly moderately rounded grains (EM up to 60%), accompanied by well-rounded grains (RM; up to >30%), which characterizes mainly coarse grains (200 to 500 μm). However, the proportions of shiny grains (EM/EL) decrease. The scanning electron microscopy (SEM) analysis discloses quartz sand grains, well-rounded with low relief having smooth surfaces in view of abrasion. Furthermore, bulbous edges, crescent percussion marks (aeolian pitting) and elongated depressions (dish-shaped concavities) can be observed in Fig. 5B to D. The aeolian features of the above microtextures suggest strong wind energy at the time of sedimentation.

Chemical action also seems to have played a significant role, as revealed in the form of partial dissolution and precipitation of quartz. This is evidenced through the presence of silica precipitations on the quartz grain surfaces being mostly due to silica flowers and silica globules (Fig. 5A). However, many quartz grain surfaces were affected with pits corroded by chemical

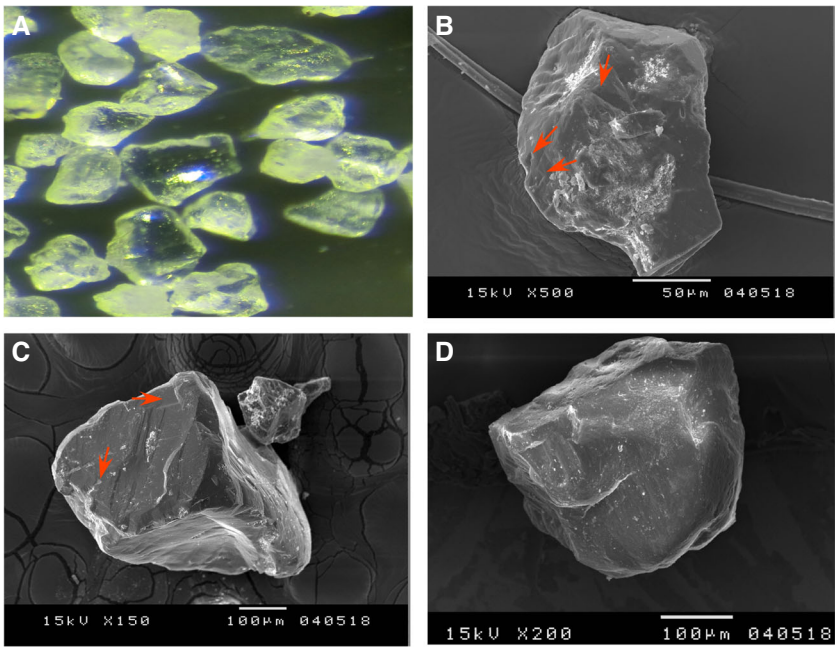

Fig. 4. Optical micrographs (A) and scanning electron micrographs (B), (C) and (D) of fluvial quartz grains from core Ml. (A) Angular to subangular grains with entire surface smooth and shiny. (B) Subangular grain showing V-shaped percussion cracks (see the arrows), crystalline overgrowths and chemical scaly exfoliations (at 4 cm depth). (C) Angular grain showing fractures forming straight steps and V-shaped percussions (see the arrows) (at 62 cm depth). (D) Subangular grain showing straight grooves and V-shaped percussions (at 112 cm depth).

weathering, as well as oriented etch pits occurring on most quartz grains especially on those extracted from more saline layers (Figs 5B, 5C, 6B and 6D). Chemical scaly exfoliations are also illustrated in Fig. 6B and C, indicating a high erosive water–chemical environment of the Sebkha el Melah.

Magnetic susceptibility variabilities

Magnetic susceptibility measurements of sediment samples varied from -14.5×10^{-6} SI to 156×10^{-6} SI along the Ml core (Fig. 7). Indeed, negative values were recorded in the first centimetres of surface sediments (-7.88×10^{-6} SI) followed by a rapid increase to reach their maximum of approximately 156×10^{-6} SI between 3 cm and 10 cm deep. Furthermore, from 11 to 117 cm deep, the values of the MS fluctuate between 10 and 50×10^{-6} SI before falling again at the bottom level (at 118 to 146 cm depth: Unit I) where they display negative records. Variation of these values is accounted for in terms of diamagnetic effects (for example, calcite, quartz and feldspars), paramagnetic (for example, amphibole, pyroxene, olivine and clay) and ferromagnetic minerals (for example, magnetite, titano-magnetite, goethite and hematite). It is noteworthy that iron oxides and heavy minerals (for example, ilmenite, hematite, magnetite, garnet, rutile and pyroxene) were recognized at depths that strictly correlated to the MS curve's peaks. Lower MS values at the huntite level dominate Unit I. Indeed, the gypsum-rich and halite levels (diamagnetic) suggest a lower influx of magnetic minerals into the basin during the warm periods of high salinity.

Geochemical data

Evaporite mineral concentration variabilities in the sediment profile of Ml core

The sediment profile of Ml core is characterized by an alternation of high and low content of halite and gypsum crystals (Fig. 7). Noting that the $CaCO_3$ content does not exceed 8%, calcium reflects amounts of gypsum throughout the Ml core. High Ca and S concentrations are observed at 35 to 39 cm and 87 to 123 cm depths. Sodium records an increase at 0 to 4 cm, 12 to 23 cm, 71 to 80 cm and 90 to 100 cm of depths (Fig. 7).

Potassium exhibits high proportions at the huntite level (between 124 cm and 146 cm depth), which abruptly decreases up to 123 cm depth of Ml core (where it does not exceed 1.2%). From this perspective, variation curve shape is consistent with the MS curve between

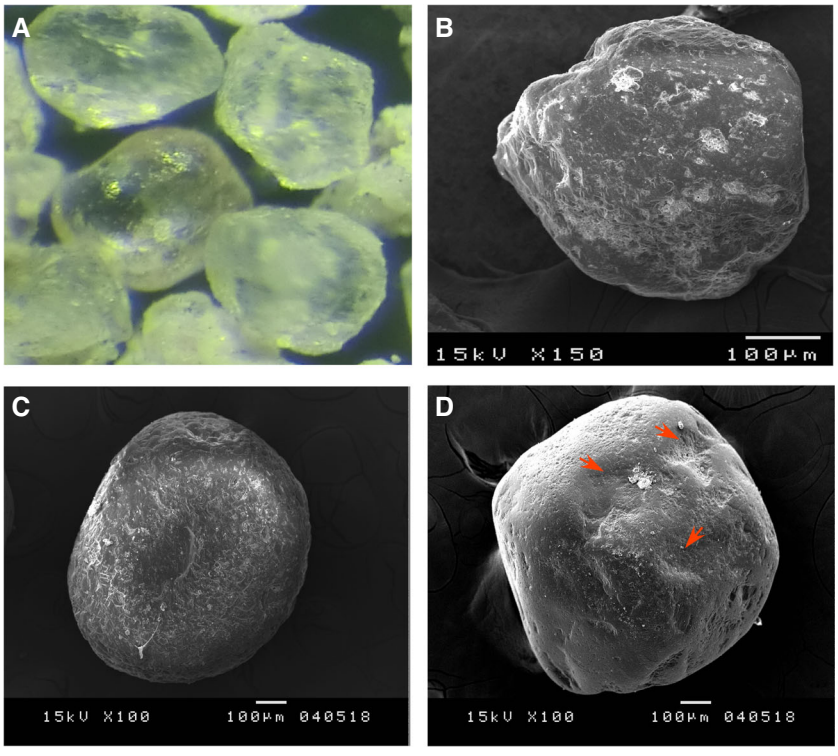

Fig. 5. Optical micrographs (A) and scanning electron micrographs (B), (C) and (D) of aeolian quartz grains from core Ml. (A) Well-rounded and moderately rounded grains with completely matt surface (40 cm depth). (B) Rounded grain with low relief, bulbous edges, crescentic percussion marks and oriented etch pits (at 40 cm depth). (C) Well-rounded grain with graded arc in the centre, crescentic percussion marks and dissolution features (at 103 cm depth). (D) Well-rounded grain with bulbous edges and dish shaped percussion marks (see the arrows) (at 103 cm depth).

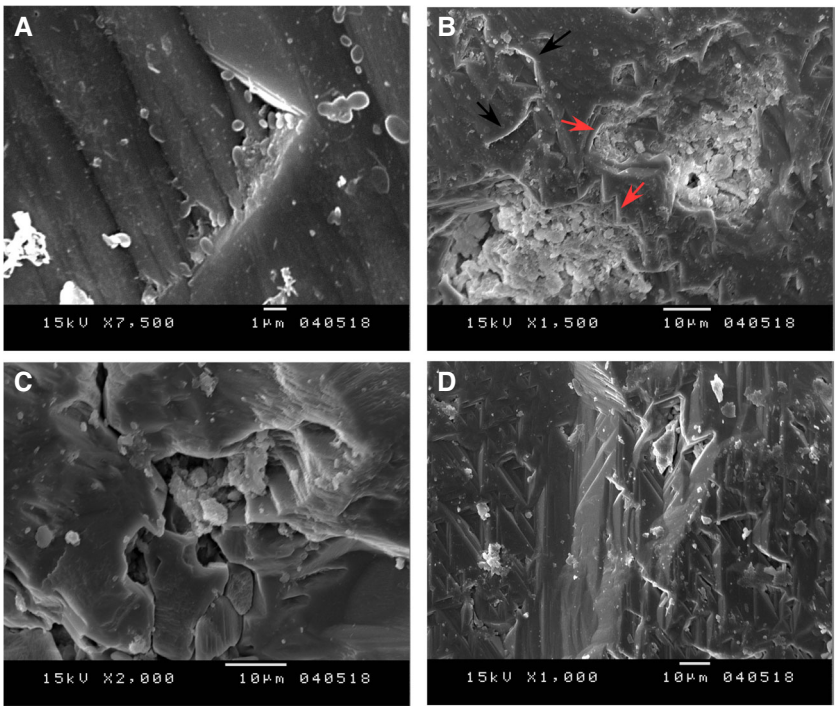

Fig. 6. Scanning electron micrographs of quartz grains from core Ml. (A) Detail of different stadia of silica precipitation, silica globules and silica flowers (at 112 cm depth). (B) Surface alteration seen in the form of surface etching (red arrows), Crescentic percussion marks can be observed (black arrows) (at 40 cm depth). (C) Surface with chemical scaly exfoliations and cracked plates caused by intense chemical weathering (at 103 cm depth). (D) Oriented etch pits (at 103 cm depth).

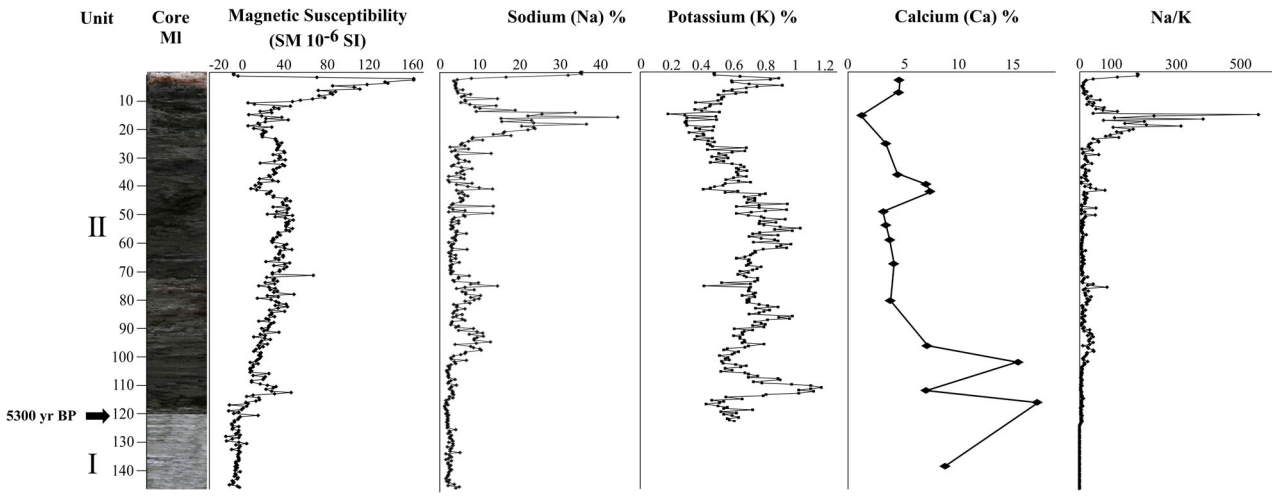

Fig. 7. Distributions of Ca, Na, K, MS and Na/K along the Ml core.

0 cm and 120 cm depth. However, enrichment of K in Unit I refers to the occurrence of the highly soluble evaporite mineral polyhalite.

Sodium content data, which represent halite concentrations, display a significantly decreasing trend. In Unit II, Na content is relatively high with maximum values reaching 40% between 12 cm and 23 cm depth and in the uppermost centimetres of the core (0 to 2 cm). In Unit I, Na exhibits the lowest concentrations with *ca* 1.5%.

The ratio Na/K serves to palaeosalinity reconstruction (Fig. 7). The maximum salinity values lie at 24 to 14 cm and 0 to 2 cm depth (the top of Unit II) and minimum values are downwards of the core (Units I and II).

Geochemical elements and reported variabilities

Major elements [Si, Fe, Ti, Mg and Al (in %)] and trace elements [Rb and Zr (in ppm)] are plotted against MS in Fig. 8. Very similar distributions of these terrigenous elements and the MS are observed, which further confirms that the elements are of the same origin. The

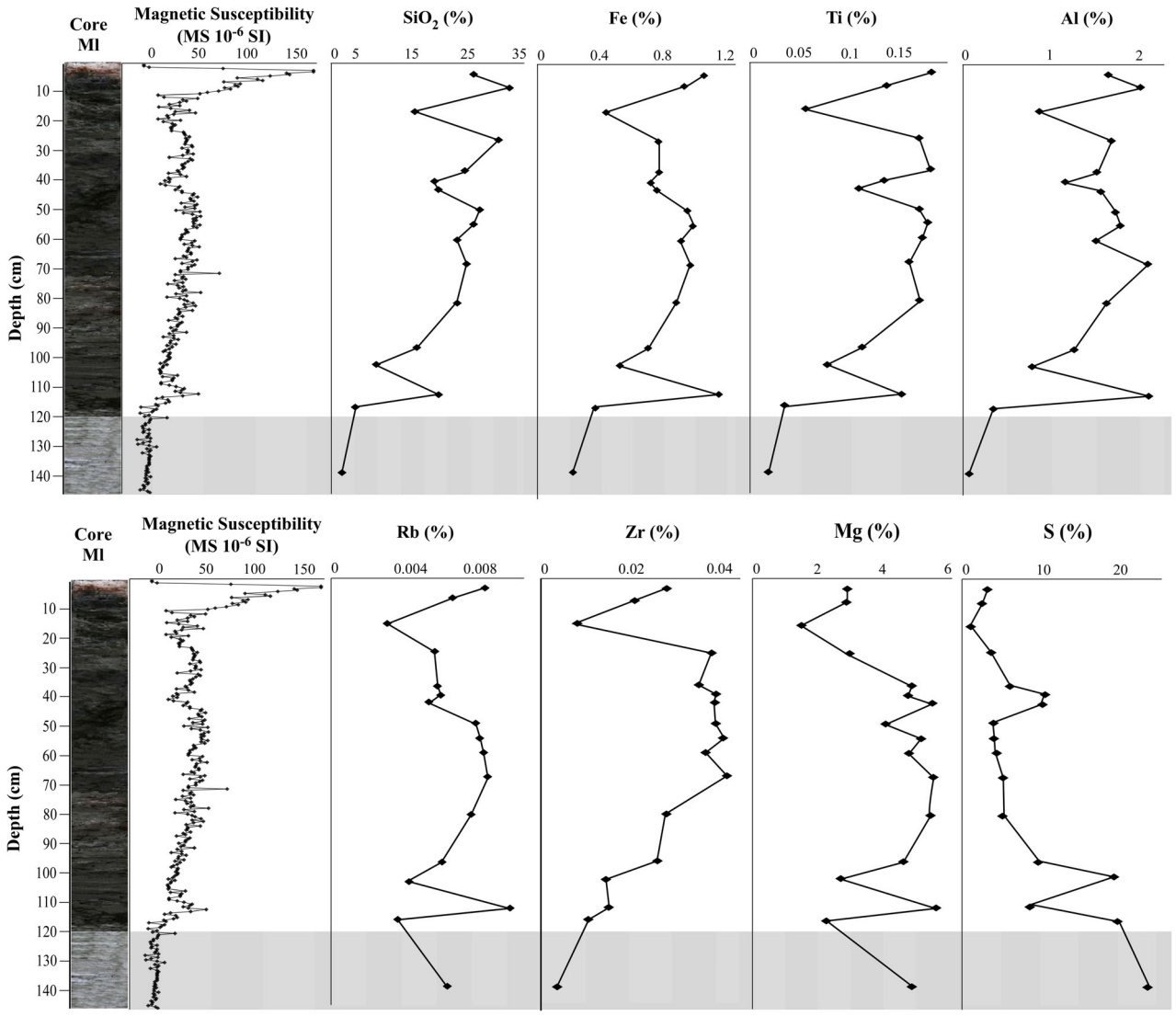

Fig. 8. Vertical geochemical distribution of major, trace elements and MS in Ml core.

concentrations of Fe (0.09 to 2%), Ti (0.01 to 0.2%), Al (0 to 2%) and Zr (0.002 to 0.05%) are highly correlated amongst themselves (see Fig. 3) and with SiO_2 content (1.6 to 33%; Units II). The lowest concentrations of Fe (0.09%) Ti (0.01%), Al (0%) and Zr (0.003%) are marked at the bottom of the Ml core, between 116 cm and 146 cm (Unit I: huntite level), at 102 cm and at 15 cm depth. However, a clearly opposite distribution of Mg and Rb is inferred at the huntite level.

The selected Zr/Al_2O_3, SiO_2/Al_2O_3, Fe/Ca and Rb/S ratios present major terrigenous fluctuations over the last 5000 years in the Sebkha el Melah (Fig. 9). The Zr/Al_2O_3 ratio displays a significant increase in facies 2 and 4. Higher values are recorded commonly with low MS signals at 116 cm, 59 cm and 39 cm depth. A considerable decrease in this ratio occurs at 15 to 8 cm, 112 cm, and between 116 cm and 146 cm depth. The Rb/S ratio demonstrates comparable distribution with the MS curve. The significant peaks at 112 cm and between 80 to 49 cm and 36 to 17 cm depth coincide with high MS signals.

A principal component analysis (PCA) was carried out in an attempt to characterize the climate variability in the geochemical dataset and to assess whether the used proxies show a distinct response of sediment provenance. This analysis was applied on a correlation matrix of major and trace elements (Fe, Si, Al, Ti, Rb, S and Zr), Si/Al_2O_3, Rb/S, Zr/Al_2O_3 and Fe/Ca in addition to the MS (Fig. 10). The result allowed to distinguish two significant axes which

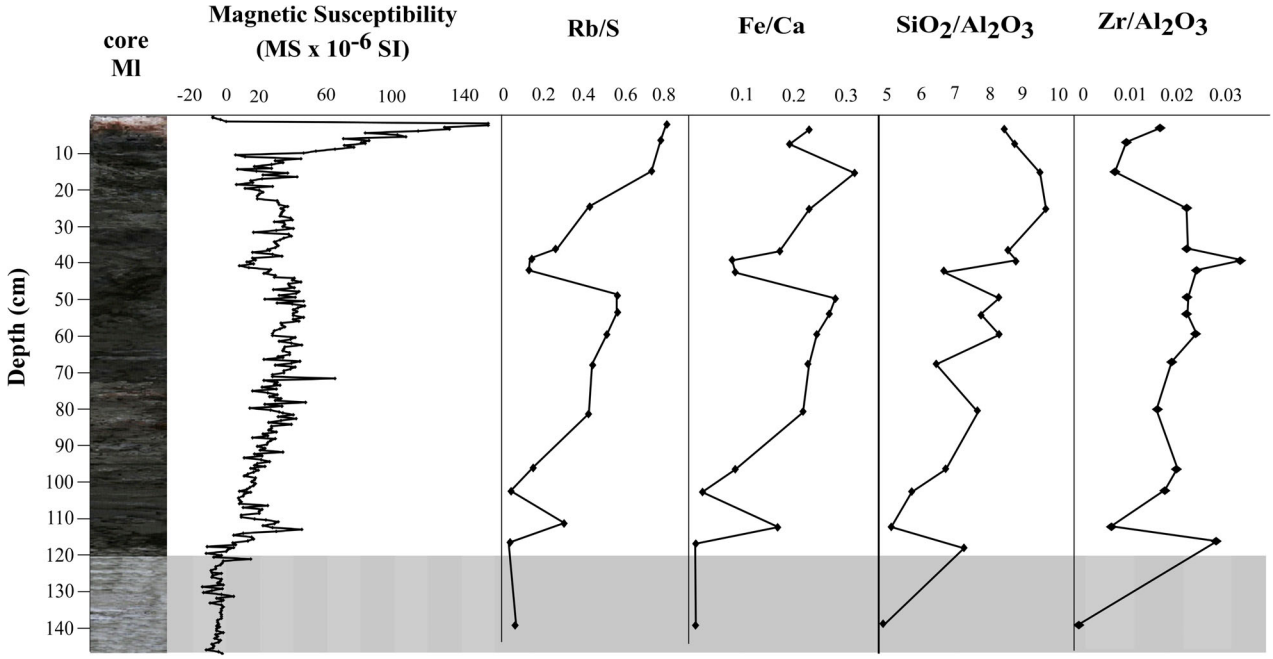

Fig. 9. Variation of Zr/Al_2O_3, SiO_2/Al_2O_3, Fe/Ca and Rb/S versus MS along the depth profile.

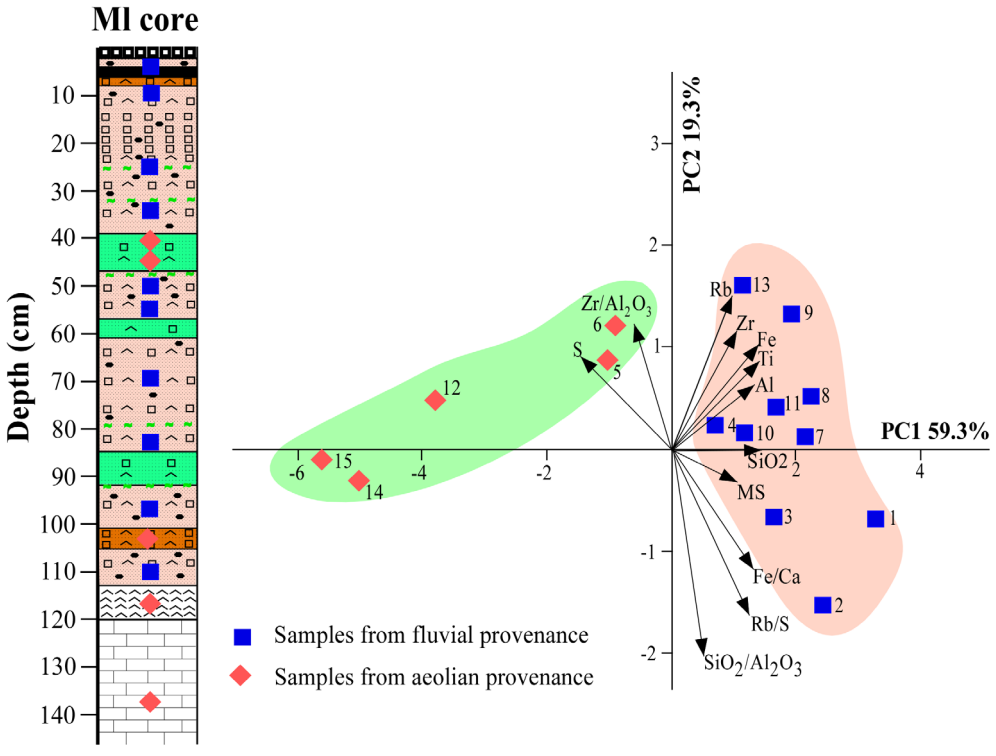

Fig. 10. Principal component analysis of geochemical and MS data from the Ml core.

together express *ca* 79% of the observed variance. The first principal component PC1 explains 59.3% of the total variance. It shows a positive correlation with Zr/Al_2O_3, S, Zr and Rb, and an anti-correlation with MS, Fe/Ca, Rb/S and Si/Al_2O_3. The second principal component

(PC2) accounted for 19.3% of the total variance and is characterized by positive loadings of MS, SiO_2, Al, Ti and Fe whereas the Zr/Al_2O_3 and S are negatively correlated. These findings reveal the existence of two distinct data groups. The MS is clearly related to the ferromagnetic group of samples and further matches the silty sediments. Zr/Al_2O_3 and S are associated with the second group of samples taken from sandy silt sediments. Therefore, two lithofacies are distinguished: (i) sediments from fluvial provenance (Facies 3); and (ii) sediments from aeolian provenance (Facies 2 and 4) (discussed below).

Mineral and geochemical composition of huntite level

Figure 11 shows the X-ray diffraction pattern of huntite (32%), this analysis indicates that Sebkha el Melah huntites are associated with polyhalite (45%), halite (11%), aragonite (7%) and dolomite (5%). A list of major and trace elements of huntites analysed by XRF is depicted in Table 1. The most prominent elements are below detection limits (Table 1). However, sulphur is the most dominant element (24%), followed by potassium and calcium (up to 8%), as it mirrors the abundance of polyhalite and huntite. Magnesium and chloride display comparable concentrations (up to 4%) and are associated also with huntite, sylvite, dolomite and halite.

DISCUSSION

Lithofacies and depositional environments

Resting upon basic sedimentological data, mean grain-size distribution, MS and content of evaporite minerals as well as microtexture of quartz grains, six main facies (F1 to F6) were recognized from the base to the top of Ml core (Table 2; Fig. 2).

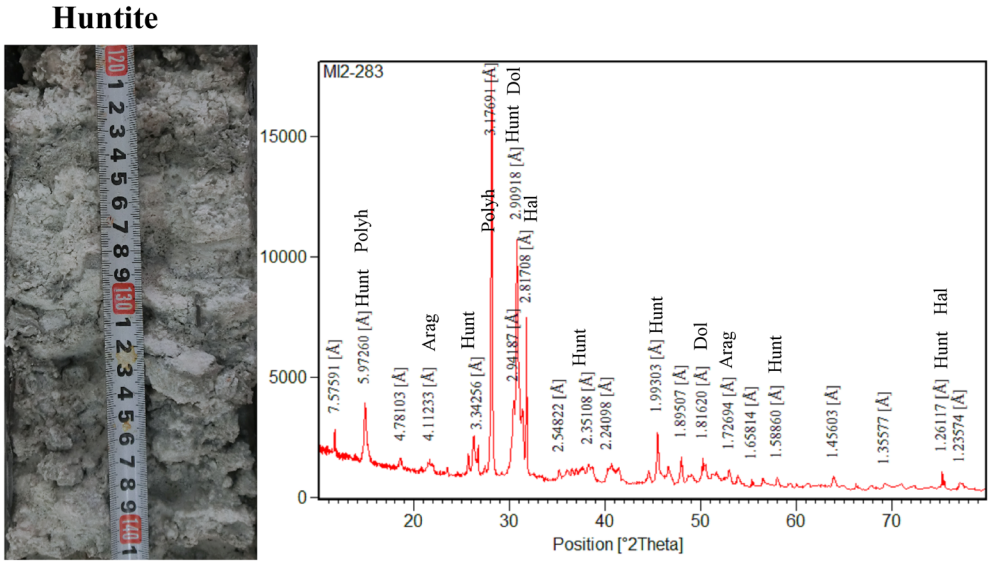

Fig. 11. X-ray diffraction pattern of el Melah huntite.

Table 1. Chemical composition (major and trace elements in ppm) of the huntite level (at 139 cm depth).

Elements	**Sb**	**Sn**	**Cd**	**Ag**	**Mo**	**Nb**	**Th**	**Zr**	**Y**	**Sr**	**U**	**Rb**	**Bi**	**As**	**Au**
Mass (ppm)	21.4	–	–	–	–	–	10.71	29.6	–	19.361	12.2	65	–	–	–
Elements	**Se**	**Hg**	**Ga**	**Pb**	**W**	**Zn**	**Cu**	**Ni**	**Co**	**Fe**	**Mn**	**Cr**	**V**	**Ti**	**Ca**
Mass (ppm)	–	–	–	–	–	–	–	–	–	953.8	–	–	–	158	86 740
Elements	**K**	**Ba**	**Al**	**P**	**Si**	**Cl**	**S**	**Mg**							
Mass (ppm)	89 494.1	–	–	–	7862.6	46 293	241 631.5	49 062.7							

Succession of climatic events during the second half of the Holocene

The facies identified in the Ml core characterize sediments deposited in the Sebkha el Melah, and allow understanding and documenting the filling history of the basin since 5000 years BP.

In fact, at 5000 years BP, the huntite level was formed under a marine/evaporite environment during the initial stages of sebkha formation. At this date, hypermagnesian carbonates overlaid the lagoonal deposits when sea level started to drop. As a matter of fact, el Melah lagoon became hypersaline and evolved into the present-day Sebkha el Melah (Davaud *et al.*, 1996).

The hypermagnesian carbonate mud exists both in the Sebkha el Melah and in the Sebkha Boujmal (which is located 15 km south of Sebkha el Melah). The thickness of this white mud amounts to 26 cm. It lies at the bottom of Ml core and it is made up of a pure huntite [$Mg_3Ca(CO_3)_4$].

At this level, the high contents in Mg and K (Table 1) are explained by the strong evaporation of stagnant waters in the el Melah depression, especially in the peripheral area following not only the marine regression dated since *ca* 5000 years BP (e.g. Jedoui *et al.*, 1998; Lakhdar *et al.*, 2006; Zaibi *et al.*, 2012; Mauz *et al.*, 2015a; Vacchi *et al.*, 2016) but also the isolation of the depression from the sea. Therefore, the polyhalite has been formed diagenetically by the transformation of gypsum in the presence of solutions rich in Mg and K (Holser, 1966). Perthuisot *et al.* (1990) demonstrated that precipitation of huntite is mediated by sulphate-reducing bacteria. Bacterial reduction, thus, destroys a part of the initially formed gypsum and prolongs the formation of carbonates (Perthuisot, 1975).

However, low trace element contents are due to the almost absence of detrital fractions (Si, Fe, Al and Ti <1%) in the massive huntite of the Sebkha el Melah. Lakhdar (2009) described the formation of hypermagnesian carbonates in the central part of the Sebkha Boujmal. It is composed mainly of huntite, magnesite ($MgCO_3$) and gypsum. Note that this level is also devoid of detrital material.

In the literature, the general chemical composition of magnesium-bearing rocks is related to the composition of the mineralizing fluids and, during evaporation and concentration of the solutes, it is associated with the composition of the brines. Stamatakis (1995) reported limited trace element contents of huntite from huntite–hydromagnesite assemblages in Kozani basin, Greece. A similar study was performed by Kuscu *et al.* (2018) in Egirdir–Hoyran lake basin (southern Turkey). These authors demonstrated relatively lower, major and trace element contents in huntite deposits. However, Yavuz *et al.* (2006) highlighted high, major and trace element contents in the Yalvac–Yarikkaya huntite deposits (Turkey) due to differences in terms of sources in the basin. In Sebkha el Melah, the presence of huntite and near absence of major and trace elements are suggestive of confined environment deposits, evaporative paragenesis and very warm and arid climate during the mid-Holocene.

Above the huntite level, a compact, decimetric gypsum crust is presented as flat crystals. This facies contains a relatively small amount of detrital sediments (silt and sand). In fact, the teardrop pattern of evaporite el Melah basin facies (Fig. 1D), showing the gypsum precipitation in the most mainland part of the basin, suggested that it was substantially sealed off from the sea (Perthuisot, 1974). Therefore, the huntite and lamellar gypsum deposits have been synchronous with the beginning of mid-Holocene marine regression in south-eastern Tunisia (Perthuisot *et al.*, 1990; Jedoui, 2000; Morhange & Pirazzoli, 2005). Moreover, the increased Zr/Al_2O_3 ratio (Fig. 12) probably coincided with a strong aridity which made the aeolian activity more efficient during warm and dry conditions. Thereby, in the lamellar gypsum facies, the peak of Zr/Al_2O_3 suggests enhanced Saharan sand deposition in the Sebkha el Melah at *ca* 5000 years BP.

Then, siliciclastic materials, originating sometimes from either wadis or wind and occasionally rich in halite or in gypsum minerals, have been succeeded from the middle to the late Holocene (Fig. 10). Indeed, since the onset of Unit II (*ca* 5300 years BP), significant depositional changes in the system were characterized by the intercalation of grey and dark grey silt and evaporite sedimentation (Unit II), above the huntite level (Unit I). Six depositional facies have been identified in Unit II, based on lithological characteristics, revealing variation in sedimentological conditions and climatic changes.

Hydrological deposits (Facies 3)

The geophysical, geochemical and sedimentological data allow identifying alternative phases of hydrological – aeolian influence (Fig. 12, blue and yellow bars) in the Sebkha el Melah. The

Table 2. Lithofacies, description and interpretation of aeolian, fluvial and sabkha facies associations in the study area.

Unit	Facies	Sedimentological features	Interpretation	Depositional environment
Unit I		Huntite horizon [$CaMg(CO_3)_4$]: white and sticky muds, named 'butter cream' by Busson & Perthuisot (1977) and Perthuisot *et al.* (1990), absence of the siliciclastic fraction, MS values are very low	Huntite is formed in a closed lagoon by sulphate reduction bacteria, from Mg-rich waters under arid to semi-arid climatic conditions (Perthuisot *et al.*, 1990)	Closed lagoon
Unit II	Facies F1	Lamellar gypsum: gypsum-rich facies in blackish silt layers. MS values are also very low	The formation of lamellar structures is probably the result of increasing salinity during dry climate, where much water is left in the basin when the evaporation rate is high and consequently gypsum is deposited	Sebkha–lagoon
	Facies F2	Poorly sorted grey fine sands (fine sand). MS values are generally higher than those of UI and F1 (from 30 to 60 10—5 SI units), quartz grains are mainly EM/RM with crescentic percussion marks and bulbous edges and high gypsum concentration	Detrital input from intense aeolian deposition processes in warm conditions	Sebkha
	Facies F3	Very poorly sorted silts (polymodal), characterized by continuous sedimentation consisting of alternation between light and dark-grey laminae; MS values are quite high; quartz grains have mostly angular to sub-angular and shiny EM/EL with conchoidal fractures and V-shaped percussion cracks; salt and gypsum crystals are small	Detrital input from low-energy wadi deposit	Sebkha
	Facies F4	Moderately sorted silt, low MS and small salt and gypsum crystals; quartz grains are formed by EM/RM shape	Aeolian sediments with low-energy transportation	Sebkha
	Facies F5	Blackish microbial mat interbedded within very poorly sorted silty fraction containing halite crystals; MS values are very high	Cyanobacterial structures formed after high sedimentation rates caused by a stronger flood (e.g. Noffke *et al.*, 1997; Lakhdar *et al.*, 2006)	Sebkha
	Facies F6	Halite layer	Salt crust suggests intense evaporation at the sebkha surface	Sebkha

hydrological events are characterized by very poorly sorted finer clastic particles, polymodal grain-size frequency distribution curves, AL/EL quartz grains with V-shaped percussion cracks, increasing trend in MS reflecting the enhanced riverine input from the catchment at the site (an increased trend of fluvial derived-elements: Si, Fe, Ti, Al, Mn and Mg, associated with the heavy minerals fraction), and the relatively high values of the Fe/Ca and Rb/S ratios (Fig. 10; elemental ratios, such as K/Al, Mg/Al, Rb/Al, Al/Na, Al/Ca, Rb/S and Ti/Al) which have been particularly useful as proxies for fluvial input (e.g. Roy *et al.*, 2008; Nieto-Moreno *et al.*, 2011; Martinez-Ruiz *et al.*, 2015; Degeai *et al.*, 2017). Nine extreme hydrological events (HE; Fig. 12: HE1 to HE9) are determined in the sediments of the Sebkha el Melah, since the mid-Holocene, reflecting an increase in flood intensity. All of these events are associated with facies 3 which dominates Unit II. The MS profile for the studied core shows significant enhancement in

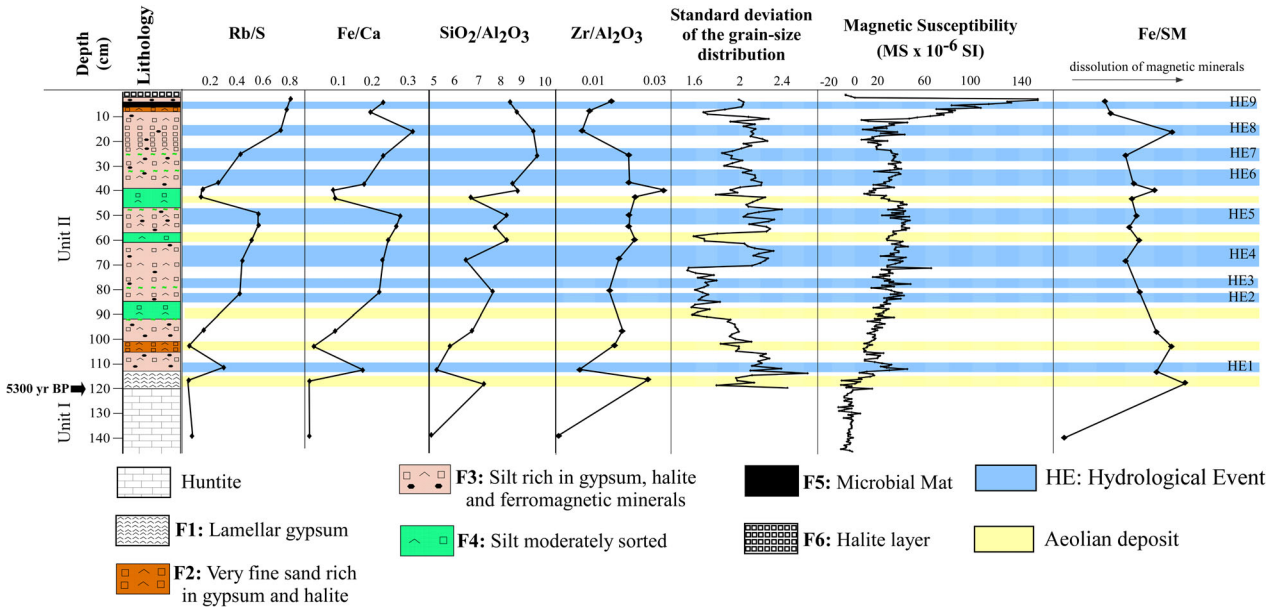

Fig. 12. Age–depth profile of detrital proxies (Rb/S, Fe/Ca, SiO_2/Al_2O_3 and Zr/Al_2O_3 ratios), MS, standard deviation of the grain-size distribution and Fe/SM is a proxy for dissolution of magnetic minerals for core Ml; blue bars indicate hydrological events and yellow bars indicate aeolian deposits.

magnetization from 2 to 9 cm deep, followed by a rapid decrease with depth. The recent depositional event HE9 is magnetically different from the rest, being composed of red laminated silts and the highest MS values (*ca* 160 × 10^{-6} SI). The other hydrological events (HE8 to HE1) display characteristically median MS values (*ca* 50 × 10^{-6} SI). A comparison of magnetic records between Sebkha el Melah and Mhabeul (situated at *ca* 7 km north of Sebkha el Melah) sediments reveals that MS values are substantially higher in the Sebkha Mhabeul (<100 × 10^{-6} SI) during the last *ca* 5000 years (see Ben Ameur *et al.*, 2021). This suggests that the relatively low MS values from the HE1 to HE8 sediments represent a response to the variations of the magnetic properties in the mid-late Holocene sequence. This decrease in MS can be explained by: (i) an increase of evaporitic minerals concentration; and (ii) an increasing dissolution of magnetic minerals.

In fact, it is likely that magnetic mineral deposition (in HE1 to HE8) is strongly affected by evaporite production (increased evaporite content dilutes MS). At Sebkha el Melah, Na values ranging between 30 and 400 g kg^{-1}, indicate that there is a high contribution of marine-derived evaporite materials. However, relatively low values of halite content are recorded in Sebkha Mhabeul (maximum 60 g kg^{-1}, Ben Ameur *et al.*, 2021), which is completely separated from the sea. Therefore, in Sebkha el Melah, the variation in MS is influenced by concentration variations of the diamagnetic minerals. Da Silva *et al.* (2013) concluded from the comparison they established between MS trends and palaeoenvironmental indicators (facies), as well as detrital input proxies, that diagenesis, remagnetization and the higher content of diamagnetic minerals can potentially obscure the MS signal of original deposits. Likewise, several researchers argued that environmental causes such as reducing sedimentary environments (e.g. Maher & Thompson, 1995; Florindo *et al.*, 2003; Nowaczyk *et al.*, 2007; Rowan *et al.*, 2009), anoxic sulphidic conditions (e.g. Florindo *et al.*, 2003; Ortega *et al.*, 2006; Nowaczyk *et al.*, 2007) and high dissolved silica concentration (e.g. Carter *et al.*, 1999; Florindo *et al.*, 2003) favour dissolution of magnetic iron oxides yielding low susceptibility values.

In order to identify iron mineral alterations by early diagenesis processes (or chemical weathering), Fe/MS ratio has been used in this study (Fig. 12). This ratio reveals the dissolution of ferrimagnetic minerals, as the denominator strictly measures ferrimagnetic minerals (e.g. Robinson *et al.*, 2000). In the Ml core, the highest values of MS occur between 3 cm and 10 cm depth, corresponding to a very low Fe/MS ratio

owing to almost zero of magnetic minerals dissolution. However, sediments between 10 cm and 22 cm depth show a significant decrease in MS and increase in Fe/MS values, which possibly indicates a transient change in magnetic mineralogy at the beginning of the Present time. This level is also marked by highest halite concentrations (Fig. 7), which accelerates chemical weathering. Iron/MS ratio continues to gradually increase with depth (Unit I: 120 cm: huntite level), whereas MS values decrease.

Thus, it is noteworthy that the most significant peaks in the magnetic mineral dissolutions of the core Ml occur within the evaporite-rich sediments (at 15 cm, 40 cm, 101 cm and 116 cm depth, Fig. 7). The hydro-sedimentary influx events (HE1 to HE8) correspond to relatively humid periods. During these periods, flooding of the surface by intense rainfall events causes dissolved salts (positive hydrological pattern), which lowers salinity and, therefore, magnetic minerals dissolution.

The microtexture analysis of quartz grain surfaces clearly demonstrates a relatively high chemical weathering. Chemical scaly exfoliation and oriented etch pits are present in almost all quartz grain surfaces, covering sometimes more than 50% of the grain (Fig. 6). The chemical alteration causes widespread disintegration on the grain surface and defects within the crystal lattice. These data denote that the most intense chemical weathering correlates with sediments of marked evaporite concentrations, indicating strong post-sedimentary processes or early diagenetic features. Thus, it can be deduced that chemical weathering which might relate to the high erosive chemical environment and anoxic phases of the sebkha lead to magnetic minerals dissolution.

Aeolian activity records

Conversely, in Sebkha el Melah, the aeolian sand inputs, corresponding to facies 4 and facies 2 (see Fig. 12, yellow lines), are indicated by low MS values, high contents of round matt grains with crescentic percussion marks, high Zr/Al_2O_3, SiO_2/Al_2O_3 ratios (proxies to reconstruct the aeolian input, e.g. Roy *et al.*, 2006, 2008, 2009; Calvert & Pedersen, 2007; Nieto-Moreno *et al.*, 2011; Martinez-Ruiz *et al.*, 2015) and are confirmed by granulometric characteristics of aeolian transport (better sorted coarser clastic particles). Indeed, detailed studies of grain-size distributions of clastic sediments carried out by Qiang *et al.* (2010), Sun *et al.* (2002, 2004) and Jiang & Ding (2010), emphasize that the particle size distribution curves of wind deposits are often bimodal. Hence, five aeolian deposits (Fig. 12) were reconstructed relying on the above sedimentary proxies.

All of the sampling points of SEM, which present obvious aeolian origin, have better sorting and bimodal grain-size frequency curves (suggesting aeolian deposits). This pattern of grain-size distribution is similar to that of the aeolian sand in the nearby Sebkha Mhabeul sediments (Ben Ameur *et al.*, 2019). The sediments of the Sebkha el Melah are sourced from Matmata loess Plateau (Fig. 1), where significant deposits of peri-desert loess originate from the Sahara (Great Eastern Erg) and are accumulated on Matmata by wind action during the Quaternary (Coudé-Gaussen & Rognon, 1988).

The Saharan platform (southern Tunisia) so called: 'Grand Erg oriental' is a major source of sand to the Jeffera coastal plain (Coudé-Gaussen, 1991; Swezey *et al.*, 1999; Giraudi, 2005; Ben Fraj, 2012; Giraudi *et al.*, 2012) owing to a strong Saharan wind, which is basically recurrent in spring and summer. In southern Tunisia, Ballais *et al.* (1979) suggested a progressive climatic aridification beginning during mid-Holocene and a mobilization of aeolian sands due to desertification.

The fluvio-aeolian succession in Sebkha el Melah, can be regarded as the result of a climate change. The change from fluvial deposits to aeolian deposits suggests a shift from relatively humid to more arid conditions. From this perspective, this study indicates that Sebkha el Melah sedimentation was characterized by an enhanced supply of Saharan sand during warmer periods (high evaporite mineral concentrations) and a decreased supply or absence of Saharan deposits during colder or less warm periods. During warm periods, intense aeolian activity resulted in frequent reworking of aeolian sand from Matmata Mountains owing to a reduced fluvial discharge and an overall lowering of the water table that increased sand availability for wind transport.

The interpretation of the sand influx reconstruction as a storminess proxy is supported by comparisons with other published records from the Mediterranean regions. The results of the central and eastern Mediterranean sediments (e.g. Freydier *et al.*, 2001; Desprat *et al.*, 2013; Magny *et al.*, 2013; Wu *et al.*, 2016), support the common assertion that aeolian supply became higher after 5500 years BP.

Evaporitic facies and palaeosalinity

Evaporitic environments are marked by two distinct depositional facies, F1 in the base of Unit II as well as F6 in the uppermost part. Facies F1 is a lamellar gypsum (big crystals: some centimetres in size), formed by evaporation, concentration and crystallization of brine during the beginning periods of sebkha basin development. According to Babel (2002), the development of coarse gypsum crystals in thick crusts is commonly associated with environments of very high salinities (<200‰) where cyanobacterial activity is mitigated or inhibited. Consequently, F1 evaporitic facies is interpreted to have been deposited on the bottom of a shallow saline pan under: (i) hypersaline conditions; and (ii) extreme arid climate combined with a scarcity of local freshwater inflow. Facies F6 occurs as a white crust of pure halite crystals, reaching 30 m thick at the centre of the depression (Perthuisot, 1971). It was precipitated at the surface from supersaturated standing brines. In the northern edge of Sebkha el Melah (Ml core location), the white salt crust is formed of polygonal ridges on the surface of the brine. This salt crust (2 cm) is precipitated by evaporation of groundwater discharge or as crusts accumulate by the evaporation to dryness of ephemeral ponds of storm-driven marine brines.

The vertical changes in depositional facies, and high resolution study of geochemistry records from the Ml core, make it possible to reconstruct the Sebkha el Melah evolution in response to sea-level fluctuations and climatic factors. In this research, the evaluation of palaeosalinity changes in the Sebkha el Melah basin since the mid-Holocene has been established using the Na/K elemental proxy as an indicator of sea-level change according to Lopez-Buendia *et al.* (1999; Fig. 7). Thus, Na/K demonstrates very low variability at Unit I and at the base of Unit II, increasing towards the top of Unit II. Therefore, since the mid-Holocene, the main salinity changes at the Sebkha el Melah basin are related to high evaporation rather than to sea-level fluctuation. The main salinity event at 35 cm depth can be correlated with the warming Present time (last 200 years).

The sedimentology proxies of Unit II, suggest a predominantly subaerial environment. Unit II marks a clear regressive period. Additionally, the salt mineral concentrations (Fig. 7) display several oscillations, suggesting that salinity in the closed Sebkha el Melah basin is generally governed by the amount of precipitation versus evaporation. The fluctuations of the mineral salts in Unit II may correspond to the surface temperature changes. Basically, Unit II of the Ml core is characterized by high-salinity concentrations, which presumably suggest warm climate simultaneous with the episodic intrusions of salt water from the sea, due to tides, storm surges and sea-level change.

CONCLUSION

Since the middle Holocene, the depression of el Melah evolved to a closed lagoon environment. Huntite Unit I, corresponding to carbonate facies deposited during the marine regression of the second half of Holocene when the lagoon was disconnecting from the Mediterranean Sea, is described as a transitional level from lagoonal to sebkha environment. Above Unit I, at Unit II, a relatively thick lamellar gypsum level was set up indicating a hot and dry climatic period which probably coincided with the Bronze Age (5000 to 3200 years BP). Then, the late Holocene represents the development stage of a modern coastal sabkha. It was marked by an alternation of fluvio-aeolian deposits that were associated with minerals and salts in varying concentrations. The succession of detritus-rich and evaporite-rich sediments confirms the regional climate forcing. At the top of this sedimentary sequence of el Melah sebkha, a thin layer of halite crystals precipitated during the present global warming. Thus, the evaporite deposits, in the Sebkha el Melah, represent the response of this highly sensitive area to climate change, and high salinities imply that this supratidal sebkha is under the influence of marine intrusions and coastal swash.

ACKNOWLEDGEMENTS

The authors would like to thank Pr. Ali Tlili from Faculty of Sciences of Sfax for XRF measurements. We are deeply grateful to Technopole of Borj Cedria (Laboratory of Georesources, Tunisia) for mineralogy analyses. Special thanks are due to Prof. Xiaoguang Qin (Key Laboratory of Cenozoic Geology and Environment Institute of Geology and Geophysics, Chinese Academy of Sciences) for providing the software applied to the lognormal distribution of the function

method. The authors kindly like to thank Mohamed Sghair Ben Reguiga and the "Entreprise Tunisienne d'Activités Pétrolières" (ETAP, Tunisia) for the technical support during the SEM microscopy in their facilities. The magnetic susceptibility and the grain-size distribution analyses were performed at the National Engineering School of Sfax in Tunisia. This study was financially supported by the University of Sfax and GEOGLOB Laboratory, «Géoressources, Environnement Naturels et Changements Globaux» (LR-13-ES-23). The authors wish to thank the reviewers for their incisive and helpful comments which greatly improved the original manuscript.

DATA AVAILABILITY STATEMENT

The data that support the findings of this study are available from the corresponding author upon reasonable request.

REFERENCES

Abichou, A. (2002) Landscape evolution in the catchment areas of the wadi Tataouine-Fessi (Southeast Tunisia). A multiscale and micromorphological study of sediments of sebkhas and an investigation of pellicular surface organisation. Ph.D. Thesis. Université Michel-de-Montaigne Bordeaux 3, France, 410 pp.

Babel, M. (2002) The largest natural crystal in Poland. *Acta Geol. Pol.*, **52**, 251–267.

Ballais, J.L., **Marre, A.** and **Rognon, P.** (1979) Périodes arides du Quaternaire récent et déplacement des sables éoliens dans les Ziban (Algérie). *Rev. Géogr. Phys. Géol. Dyn.*, **21**, 97–108.

Ben Ameur, M., **Masmoudi, S.**, **Abichou, A.**, **Medhioub, M.** and **Yaich, C.** (2019) Use of the magnetic, geochemical, and sedimentary records in establishing paleoclimate change in the environment of Sebkha: case of the Sebkha Mhabeul in southeastern Tunisia. *Comp. Rend. Geosci.*, **351**, 487–497.

Ben Ameur, M., **Masmoudi, S.** and **Yaich, C.** (2021) Flood and sandstorm events recorded in Holocene Sebkha deposits in Southeastern Tunisia: evidence from magnetic and geochemical properties. *Quatern. Int.*, **571**, 46–57.

Bousnina, A. (1990) Climate of Sfax. Report No. 1, Maghreb-Editions, Nat. Inst. Meteo, 61 pp.

Busson, G. and **Perthuisot, J.P.** (1977) Intérêt de la Sabkha el Melah (sud tunisien) pour l'interprétation des séries évaporitiques anciennes. *Sediment. Geol.*, **19**, 139–164.

Cailleux, A. (1942) Les actions éoliens périglaciaires en Europe. *Mém. Soc. Géol.*, **46**, 1–176.

Calvert, S.E. and **Pedersen, T.F.** (2007) Elemental proxies for palaeoclimatic and palaeoceanographic variability in marine sediments: interpretation and application. *Dev. Mar. Geol.*, **1**, 567–644.

Carter, R.M., **McCave, I.N.**, **Richter, C.** and **Carter, L.** (1999) Southwest Pacific gateways, Sites 1119–1125. In: *Proceedings of the Ocean Drilling Program, Initial Reports, 181*. Ocean Drilling Program, College Station, Texas, 80 pp.

Coudé-Gaussen, G. (1991) *Les Poussières Sahariennes, Cycle Sédimentaire et Place Dans les Environnements et Paléoenvironnements Désertiques, Edition*. John Libbey Eurotext, France, 465 pp.

Coudé-Gaussen, G. and **Rognon, P.** (1988) Caractérisation sédimentologique et conditions paléoclimatiques de la mise en place de loess au Nord du Sahara à partir de l'exemple du Sud-Tünisien. *Bull. Soc. Géol. France*, **8**, 1081–1090.

Da Silva, A.C., **De Vleeschouwer, D.**, **Boulvain, F.**, **Claeys, P.**, **Fagel, N.**, **Humblet, M.**, **Mabille, C.**, **Michel, J.**, **Sardar Abadi, M.**, **Pas, D.** and **Dekkers, M.J.** (2013) Magnetic susceptibility as a high-resolution correlation tool and as a climatic proxy in Paleozoic rocks – merits and pitfalls: examples from the Devonian in Belgium. *Mar. Petrol. Geol.*, **46**, 173–189.

Davaud, E., **Jedoui, Y.** and **Strasser, A.** (1996) Holocene peritidal and evaporitic sedimentation in southern Tunisia. *17th IAS meeting of Sedimentology, Sfax, fieldtrip guidebook*, 71–82.

Degeai, J.F., **Devillers, B.**, **Blanchemanche, P.**, **Dezileau, L.**, **Tillier, M.** and **Bohbo, H.** (2017) Fluvial response to the last Holocene rapid climate change in the Northwestern Mediterranean coastlands. *Glob. Planet. Change*, **152**, 176–186.

Desprat, S., **Combourieu-Nebout, N.**, **Essallami, L.**, **Sicre, M.A.**, **Dormoy, I.**, **Peyron, O.**, **Siani, G.**, **Bout Roumazeilles, V.** and **Turon, J.L.** (2013) Deglacial and Holocene vegetation and climatic changes in the southern Central Mediterranean from a direct land-sea correlation. *Clim. Past*, **9**, 767–787.

Florida, S. (1971) *La Sabkha el Melah de Zarzis: Géologie, Géochimie, Hydrologie*. Rapport inédit O.N.M. Tunis.

Florindo, F., **Roberts, A.P.** and **Palmer, M.R.** (2003) Magnetite dissolution in siliceous sediments. *Geochem. Geophys. Geosyst.*, **4**, 1–13.

Folk, R. and **Ward, W.** (1957) Brazos River bars, a study in significance of grain-size parameters. *J. Sed. Petrol.*, **27**, 13–27.

Fontes, J.C. and **Perthuisot, J.P.** (1971) Faciès minéralogiques et isotopiques des carbonates de la Sebkha el Melah (Zarzis, Tunisie): les variations du niveau de la Méditerranée orientale depuis 40000 ans. *Rev. Géogr. Phys. Géol. Dyn.*, **13**, 299–314.

Fontes, J.C. and **Perthuisot, J.P.** (1973) Climatic record for the past 50 000 years in Tunsia. *Nat. Phy. Sci. Londres*, **244**, 74–75.

Fraj, T.B. (2012) Proposition d'un schéma chronostratigraphique des héritages quaternaires continentaux de la Jeffara septentrionale et de la partie nord-orientale du plateau de Dahar-Matmata (Sud-est tunisien). *Quaternaire*, **23**, 187–204.

Freydier, R., **Michard, A.**, **de Lange, G.J.** and **Thomson, J.** (2001) Nd isotopic compositions of Eastern Mediterranean sediments: tracers of the Nile influence during sapropel S1 formation? *Mar. Geol.*, **177**, 45–62.

Ghedhoui, R., **Deffontaines, B.** and **Rabia, M.C.** (2016) Neotectonics of costal Jeffara (southern Tunisia): state of the art. *Tectonophysics*, **676**, 211–228.

Giraudi, C. (2005) Eolian sand in the peridesert northwestern Libya and implications for Late Pleistocene

and Holocene Sahara expansion. *Palaeogeogr. Palaeoclimat. Palaeoecol.*, **218**, 161–173.

Giraudi, C., **Mercuri, A.M.** and **Esu, D.** (2012) Holocene palaeoclimate in the northern Sahara margin (Jefara Plain, northwestern Libya). *Holocene*, **23**, 339–352.

Holser, W.T. (1966) Diagenetic polyhalite in recent salt from Baja California. *Am. Minerol*, **51**, 99–109.

Jedoui, Y. (2000) Sédimentologie et géochronologie des dépôts littoraux quaternaires: reconstitution des variations des paléoclimats et du niveau marin dans le Sud-Est tunisien. PhD Thesis State. Faculty of Science of Tunis, Tunisia, 338 pp.

Jedoui, Y., **Kallel, N.**, **Fontugne, M.**, **Ben Ismail, M.H.**, **M'Rabet, A.** and **Montacer, M.** (1998) A high relative sea level stand in the middle Holocene of southeastern Tunisia. *Mar. Geol.*, **147**, 123–130.

Jiang, H.C. and **Ding, Z.L.** (2010) Eolian grain-size signature of the SiKouzi lacustrine sediments (Chinese Loess Plateau): implications for Neogene evolution of the East Asian winter monsoon. *Geol. Soc. Am. Bull.*, **122**, 843–854.

Kenig, K. (2006) Surface microtextures of quartz grains from Vistulian loesses from selected profiles of Poland and some other countries. *Quatern. Int.*, **152–153**, 118–135.

Krinsley, D.H. and **Doornkamp, J.C.** (1973) *Atlas of Quartz Sand Surface Textures*. Cambridge University Press, Cambridge, 91 pp.

Kuscu, M., **Cengiz, O.** and **Kahya, A.** (2018) Mineralogy and geochemistry of sedimentary huntite deposits in the egirdir-hoyran lake basin of Southern Turkey. *J. Geo. Soc. India*, **91**, 496–504.

Lakhdar, R. (2009) Les sédiments holocènes et tapis microbiens du littoral du Sud-Est de la Tunisie: Sédimentologie et paléoenvironnements. Ph.D. thesis. Faculty of Science of Sfax, Tunisia.

Lakhdar, R., **Soussi, M.**, **Ben Ismail, M.H.** and **M'Rabet, A.** (2006) A Mediterranean Holocene restricted coastal lagoon under arid climate: case of the sedimentary record of Sabkha Boujmel (SE Tunisia). *Palaeogeogr. Palaeoclimatol. Palaeoecol.*, **241**, 177–191.

Le Ribault, L. (1977) *L'exoscopie des quartz*. Masson, Paris, 150 pp.

Lopez-Buendia, A.M., **Bastida, J.**, **Querol, X.** and **Whateley, M.K.G.** (1999) Geochemical data as indicators of palaeosalinity in coastal organic-rich sediments. *Chem. Geol.*, **157**, 235–254.

Magny, M., **Combourieu-Nebout, N.**, **de Beaulieu, J.L.**, **Bout-Roumazeilles, V.**, **Colombaroli, D.**, **Desprat, S.**, **Francke, A.**, **Joannin, S.**, **Ortu, E.**, **Peyron, O.**, **Revel, M.**, **Sadori, L.**, **Siani, G.**, **Sicre, M.A.**, **Samartin, S.**, **Simonneau, A.**, **Tinner, W.**, **Vannière, B.**, **Wagner, B.**, **Zanchetta, G.**, **Anselmetti, F.**, **Brugiapaglia, E.**, **Chapron, E.**, **Debret, M.**, **Desmet, M.**, **Didier, J.**, **Essallami, L.**, **Galop, D.**, **Gilli, A.**, **Haas, J.N.**, **Kallel, N.**, **Millet, L.**, **Stock, A.**, **Turon, J.L.** and **Wirth, S.** (2013) North–south palaeohydrological contrasts in the central Mediterranean during the Holocene: tentative synthesis and working hypotheses. *Clim. Past Discuss*, **9**, 1901–1967.

Mahaney, W.C. (2002) *Atlas of Sand Grain Surface Textures and Applications*. Oxford University Press, New York, 237 pp.

Maher, B.A. and **Thompson, R.** (1995) Paleorainfall reconstructions from pedogenic magnetic susceptibility variations in the Chinese loess and paleosols. *Quatern. Res.*, **44**, 383–391.

Martinez-Ruiz, F., **Kastner, M.**, **Gallego-Torres, D.**, **Rodrigo-Gamiz, M.**, **Nieto-Moreno, V.** and **Ortega-Huertas, M.** (2015) Paleoclimate and paleoceanography over the past 20,000 yr in the Mediterranean Sea Basins as indicated by sediment elemental proxies. *Quatern. Sci. Rev.*, **107**, 25–46.

Mauz, B., **Ruggieri, G.** and **Spada, G.** (2015a) Terminal Antarctic melting inferred from a far-field coastal site. *Quatern. Sci. Rev.*, **116**, 122–132.

Morhange, C. and **Pirazzoli, P.A.** (2005) Mid-Holocene emergence of southern Tunisian coasts. *Mar. Geol.*, **229**, 205–213.

Nieto-Moreno, V., **Martinez-Ruiz, F.**, **Giralt, S.**, **Jiménez-Espejo, F.**, **Gallego-Torres, D.**, **Rodrigo-Gámiz, M.**, **García-Orellana, J.**, **Ortega-Huertas, M.** and **de Lange, G.J.** (2011) Tracking climate variability in the western Mediterranean during the Late Holocene: a multiproxy approach. *Clim. Past*, **7**, 1395–1414.

Noffke, N., **Gerdes, G.**, **Klenke, T.** and **Krumbein, W.E.** (1997) A microscopic sedimentary succession of graded sand and microbial mats in modern siliciclastic tidal flats. *Sed. Geol.*, **110**, 1–6.

Nowaczyk, N.R., **Melles, M.** and **Minyuk, P.** (2007) A revised age model for core PG1351 from Lake El'gygytgyn, Chukotka, based on magnetic susceptibility variations tuned to northern hemisphere insolation variations. *J. Paleolimnol.*, **37**, 65–76.

Ortega, B., **Caballero, M.**, **Lozano, S.**, **Vilaclara, G.** and **Rodrigues, A.** (2006) Rock magnetic and geochemical proxies for iron mineral diagenesis in a tropical lake: Lago Verde, Los Tuxtlas, East-Central Mexico. *Earth Planet. Sci. Lett.*, **250**, 444–458.

Perthuisot, J.P. (1971) Recent polyhalite from Sebkha el Melah (Tunisia). *Nat. Phys. Sci.*, **232**, 186–187.

Perthuisot, J.P. (1974) Les dépôts salins de la Sebkha el Melah de Zarzis: conditions et modalités de la sédimentation évaporitique. *Rev. Geogr. Phys. Géol. Dyn.*, **16**, 177–188.

Perthuisot, J.P. (1975) La Sebkha el Melah de Zarzis: Genèse et évolution d'un bassin salin paralique. Ecole Normale Superieure (Paris, France), Travaux Laboratoire Géologie, 152 pp.

Perthuisot, J.P., **Castanier, S.** and **Maurin, A.** (1990) The huntite of Sabkha al Melah (Zarzis, Tunisia). An example of carbonate biodiagenesis. *Bull. Soc. Géo. France*, **4**, 657–666.

Perthuisot, J.P., **Florida, S.** and **Jausein, A.** (1972) Un modèle récent de bassin côtier à sédimentation saline: la Sebkha el Melah (Zarzis, Tunisie). *Rev. Géogr. Phys. Géol. Dyn.*, **16**, 67–84.

Qiang, M., **Lang, L.** and **Wang, Z.** (2010) Do fine-grained components of loess indicate westerlies: insights from observations of dust storm deposits at Lenghu (Qaidam Basin, China). *J. Arid Environ.*, **74**, 1232–1239.

Qin, X.G., **Cai, B.G.** and **Liu, T.S.** (2005) Loess record of the aerodynamic environment in the east Asia monsoon area since 60,000 years before present». *J. Geophys. Res.*, **110**, 1–16.

Robinson, S.G., **Sahota, J.T.S.** and **Oldfield, F.** (2000) Early diagenesis in North Atlantic abyssal plain sediments characterized by rock-magnetic and geochemical indices. *Mar. Geol.*, **136**, 77–107.

Rowan, C.J., **Roberts, A.P.** and **Broadbent, T.** (2009) Reductive diagenesis, magnetite dissolution, greigite growth and paleomagnetic smoothing in marine sediments: a new view. *Earth Planet. Sci. Lett.*, **277**, 223–235.

Roy, P.D., **Nagar, Y.C.**, **Juyal, N.**, **Smykatz-Kloss, W.** and **Singhvi, A.K.** (2009) Geochemical signatures of Late Holocene paleo-hydrological changes from Phulera and Pokharan saline playas near the eastern and western margins of the Thar Desert, India. *J. Asian Earth Sci.*, **34**, 275–286.

Roy, P.D., **Smykatz-Kloss, W.** and **Sinha, R.** (2006) Late Holocene geochemical history inferred from Sambhar and Didwana playa sediments, Thar Desert, India: comparison and synthesis. *Quatern. Int.*, **144**, 84–98.

Roy, P.D., **Smykatz-Kloss, W.** and **Morton, O.** (2008) Geochemical zones and reconstruction of late Holocene environments from shallow core sediments of the Pachapadra paleo-lake, Thar Desert, India. *Geochemistry*, **68**, 313–322.

Stamatakis, M.G. (1995) Occurrence and genesis of huntite-hydromagnesite assemblages, Kozani, Greece - important new white fillers and extenders. *Trans. Instn. Min. Metall. Sect. B. Appl. Earth Sci.*, **104**, B 179–B 186.

Sun, D., **Bloemendal, J.**, **Rea, D.K.**, **Vandenberghe, J.**, **Jiang, F.**, **An, Z.** and **Su, R.** (2002) Grain-size distribution function of polymodal sediments in hydraulic and aeolian environments, and numerical partitioning of the sedimentary components. *Sed. Geol.*, **152**, 263–277.

Sun, D.H., **Bloemendal, J.**, **Rea, D.K.**, **An, Z.S.**, **Vandenberghe, J.**, **Lu, H.Y.**, **Su, R.X.** and **Liu, T.S.** (2004) Bimodal grain-size distribution of Chinese loess, and its palaeoclimatic implications. *Catena*, **55**, 325–340.

Swezey, C., **Lancaster, N.**, **Kocurek, G.**, **Deynoux, M.**, **Blum, M.**, **Price, D.** and **Pion, J.-C.** (1999) Response of aeolian systems to Holocene climatic and hydrologic changes on the northern margin of the Sahara: a high-resolution record from the Chott Rharsa basin, Tunisia. *Holocene*, **9**, 141–147.

Tyler, S.W., **Munoz, J.F.** and **Wood, W.W.** (2006) The response of playa and sabkha hydraulics and mineralogy to climate forcing. *Ground Water*, **44**, 329–338.

Vacchi, M., **Marriner, N.**, **Morhange, C.**, **Spada, G.**, **Fontana, A.** and **Rovere, A.** (2016) Multiproxy assessment of Holocene relative sea-level changes in the western Mediterranean: sea-level variability and improvements in the definition of the isostatic signal. *Earth-Sci. Rev.*, **155**, 172–197.

Vos, K., **Vandenberghe, N.** and **Elsena, J.** (2014) Surface textural analysis of quartz grains by scanning electron microscopy (SEM): from sample preparation to environmental interpretation. *Earth-Sci. Rev.*, **128**, 93–104.

Wu, J., **Böning, P.**, **Pahnke, K.**, **Tachikawa, K.** and **de Lange, G.J.** (2016) Unraveling North-African riverine and eolian contributions to central Mediterranean sediments during Holocene sapropel S1 formation. *Quatern. Sci. Rev.*, **152**, 31–48.

Yavuz, F., **Mehmet, S.K.** and **Gökhan, Ö.** (2006) The occurrence and geochemistry of huntite from Neogene lacustrine sediments of the Yalvac-Yarikkaya Basin. *Isparta. N. Jb. Miner. Abh.*, **182**(2), 201–212.

Zaibi, C., **Carbonel, P.**, **Kamoun, F.**, **Fontugne, M.**, **Azri, C.**, **Jedoui, Y.** and **Montacer, M.** (2012) Evolution of the sebkha Dreîaa (South-Eastern Tunisia, Gulf of Gabes) during the Late Holocene: response of ostracod assemblages. *Rev. Micropaléontol*, **55**, 83–97.

Manuscript received 23 December 2021; revision accepted 23 March 2022